

# A gravitational microlensing determination of continuum source size in Q2237+0305

J. S. B. Wyithe<sup>1</sup>, R. L. Webster<sup>1</sup>, E. L. Turner<sup>2</sup>, D. J. Mortlock<sup>1</sup>

<sup>1</sup> *School of Physics, The University of Melbourne, Parkville, Vic, 3052, Australia*

<sup>2</sup> *Princeton University Observatory, Peyton Hall, Princeton, NJ 08544, USA*

*Email: swyithe@physics.unimelb.edu.au, rwebster@physics.unimelb.edu.au, elt@astro.princeton.edu, dmortloc@physics.unimelb.edu.au*

Accepted Received

## ABSTRACT

Following the detection of a gravitational microlensing high magnification event (HME) in Q2237+0305A (Irwin et al. 1989; Corrigan et al. 1991) attempts have been made to place limits on the dimensions of the quasar continuum source. The analyses have studied either the observed event magnitude or the event duration. The latter approach has been hampered by a lack of knowledge about the transverse velocity of the lensing galaxy. We obtain both upper and lower statistical limits on the size of the continuum source from the observed HME using determinations of transverse velocity (Wyithe, Webster & Turner 1999b,c) obtained from the published monitoring data. Our calculations take account of the caustic orientation as well as the component of the caustic velocity that results from stellar proper motions. Our determination of source size relies on an assumed event duration of 52 days for HME, and so will be refined when more HMEs are observed. We find that the upper and lower limits on the magnified region of the continuum source are  $6 \times 10^{15}$  and  $2 \times 10^{13}$  cm respectively (99% confidence). Through consideration of the joint probability for source size and mean microlens mass we find that the mean mass lies between  $\sim 0.01M_{\odot}$  and  $\sim 1M_{\odot}$  (95% confidence).

**Key words:** gravitational lensing - microlensing - quasars.

## 1 INTRODUCTION

The object Q2237+0305 comprises a source quasar at a redshift of  $z = 1.695$  that is gravitationally lensed by a foreground galaxy with  $z = 0.0394$  producing 4 resolvable images with separations of  $\sim 1''$ . Each of the 4 images are observed through the galactic bulge, which has an optical depth in stars that is of order unity (eg. Kent & Falco 1988; Schneider et al. 1988; Schmidt, Webster & Lewis 1998). In addition, the proximity of the lensing galaxy means that the projected transverse velocity at the source is an order of magnitude higher than for a typical lens configuration. The combination of these considerations make Q2237+0305 the ideal object from which to study microlensing. Indeed, Q2237+0305 is the only object in which cosmological microlensing has been confirmed (Irwin et.al 1989; Corrigan et.al 1991).

The first confirmed high magnification event (HME) in image A had a measured rise time of  $\sim 26$  days, followed by a subsequent event that had a decline of  $\sim 3$  months. The resulting light-curve has been interpreted as a double peaked event corresponding to the source having crossed two fold caustics inside a cusp (Witt & Mao 1994), implying that

the peak was caused by a single caustic crossing. The observation thus provides an estimate of the event crossing time, and a lower limit to the event amplitude. Attempts have been made on both of these fronts to interpret the HME in terms of the size of the magnified continuum region (eg. Wambsganss, Paczynski & Schneider (1990); Rauch & Blandford 1991; Jaroszynski, Wambsganss & Paczynski 1992; Webster et al. 1991).

The amplitude of an HME is a function of source size - smaller sources produce events of larger amplitude. However, the event amplitude is also dependent on the width or strength of a caustic, a quantity that is the constant of proportionality in the near caustic approximation of Chang & Refsdal (1979). Witt (1990) termed this constant the flux factor and found that its value is distributed about a mean in the complex caustic structures that are produced by microlensing models. The mean value of the flux factor is a function of the average stellar mass in the model. Thus the event amplitudes have a distribution about an average that is model dependent. Wambsganss, Paczynski & Schneider (1990) produced a microlensing model with a mean microlenses mass of  $0.225M_{\odot}$  and found that the observed luminosity variation can be reproduced when the source

arXiv:astro-ph/9904361v2 25 May 1999

**Table 1.** Values of the total optical depth and the magnitude of the shear at the position of each of the 4 images of Q2237+0305. The quoted values are those of Schmidt, Webster & Lewis (1998).  $\kappa_*$  and  $\kappa_c$  are the optical depths in stars and in smoothly distributed matter respectively.

Image	$\kappa = \kappa_* + \kappa_c$	$ \gamma $
A	0.36	0.40
B	0.36	0.40
C	0.69	0.71
D	0.59	0.61

has a radius smaller than  $\sim 2 \times 10^{15} \text{ cm}$ . Several attempts have been made to discuss the observed HME magnitude in terms of physical models of the continuum region (eg. Rauch & Blandford 1991; Jaroszynski, Wambsganss & Paczynski 1992). The results of these calculations remain controversial. In addition, Lewis et al. (1998) employ the observed difference in spectra obtained at two different epochs to infer a continuum region that is  $\lesssim 10^{15} \text{ cm}$ , based on a blackbody accretion disk model.

A different approach is to use the observed event duration in combination with the transverse velocity to obtain an estimate of the source size. Approximate values have been obtained previously with the assumptions of a galactic transverse velocity of  $v_t \sim 600 \text{ km sec}^{-1}$  (providing the caustic velocity with respect to the source), and a perpendicular caustic crossing (eg. Irwin et al 1989; Webster et al. 1991). These analyses have yielded values for the continuum source size that are consistent with those obtained through consideration of the event amplitude.

In this work we present an analysis of the source size that is required to produce the observed event duration from model light-curves. This work follows results for the limit on the galactic transverse velocity that we have obtained previously (Wyithe, Webster & Turner 1999b,c). In this analysis we consider the effect of a stellar velocity dispersion as well as the angle of caustics with respect to the source trajectory on the caustic crossing time.

## 2 THE MICROLENSING MODEL

### 2.1 Microlensing models for Q2237+0305

Throughout the paper, standard notation for gravitational lensing is used. The Einstein radius of a  $1M_\odot$  star in the source plane is denoted by  $\eta_0$ . The normalised shear is denoted by  $\gamma$ , and the convergence or optical depth by  $\kappa$ . The model for gravitational microlensing consists of a very large sheet of point masses that simulates the section of galaxy along the image line-of-sight, together with a shear term that includes the perturbing effect of the mass distribution of the lensing galaxy as a whole. The normalised lens equation for a field of point masses with an applied shear in terms of these quantities is

$$\vec{y} = \begin{pmatrix} 1 - \kappa_c - \gamma & 0 \\ 0 & 1 - \kappa_c + \gamma \end{pmatrix} \vec{x} + \sum_{j=0}^{N_*} m^j \frac{(\vec{x}^j - \vec{x})}{|\vec{x}^j - \vec{x}|^2} \quad (1)$$

Here  $\vec{x}$  and  $\vec{y}$  are the normalised image and source positions respectively, and the  $\vec{x}_i$  are the normalised positions of the point masses.  $\kappa_c$  is the optical depth in smoothly distributed matter. To construct a microlensed light-curve Eqn 1 is solved for the macroimage magnification at many points along a predefined source trajectory through the inversion technique of Lewis et al. (1993) and Witt (1993).

For the microlensing models of Q2237+0305 presented in the current work we assume the macro-parameters for the lensing galaxy calculated by Schmidt, Webster & Lewis (1998). These values are shown in table 1. Two models are considered for the distribution of microlenses, one with no continuously distributed matter, and one where smooth matter contributes 50% of the surface mass density. Both the microlensing rate due to a transverse velocity (eg. Witt, Kaiser & Refsdal 1993), as well as the corresponding rate due to proper motions (Wyithe, Webster & Turner 1999a) are not functions of the details of the microlens mass distribution, but rather are only dependent on the mean microlens mass. We therefore limit our attention to models in which all the point masses have the same mass since the results obtained will be applicable to other models with different forms for the mass function.

Each of our models was computed for a source track of length  $10\eta_0$ . We set the minimum number of stars to be used in our models at 500. Two orientations were chosen for the transverse velocity with respect to the galaxy, with the source trajectory being parallel to the A–B or C–D axes. At each orientation, 100 simulations were made for each of the 4 images of Q2237+0305 in combination with each of the model mass distributions. The two orientations bracket the range of possibilities, and because the images are positioned approximately orthogonally with respect to the galactic centre correspond to shear values of  $\gamma_A, \gamma_B < 0, \gamma_C, \gamma_D > 0$  and  $\gamma_A, \gamma_B < 0, \gamma_C, \gamma_D > 0$  respectively.

For our analysis we assume that microlensing is produced through the combination of a galactic transverse velocity with an isotropic velocity dispersion. Moreover, we assume that the magnitude of the dispersion is the same at the position of each of the four images. For the line-of-sight velocity dispersion of the stars in the galactic bulge we take the theoretical value of  $\sigma_* \sim 165 \text{ km sec}^{-1}$ . The microlensing models presented in this work have been discussed in detail in Wyithe, Webster & Turner (1999c).

### 2.2 The effective transverse velocity and the effect of random proper motions

We define the effective transverse velocity as the transverse velocity that produces a microlensing rate from a static model equal to that of the observed light-curve. The effective transverse velocity therefore describes the microlensing rate due to the combination of the effects of a galactic transverse velocity and proper motion of microlenses.

To obtain limits on the effective transverse velocity, many simulations are made which have a sampling rate and period that are identical to the published monitoring data (Irwin et al. 1989, Corrigan et al. 1991, Østensen et al. 1996). Observational errors are also simulated. The simulations used two different estimates of the error in the photometric magnitudes. In the first case a small error was assumed (SE). For images A and B,  $\sigma_{SE} = 0.01 \text{ mag}$ , and

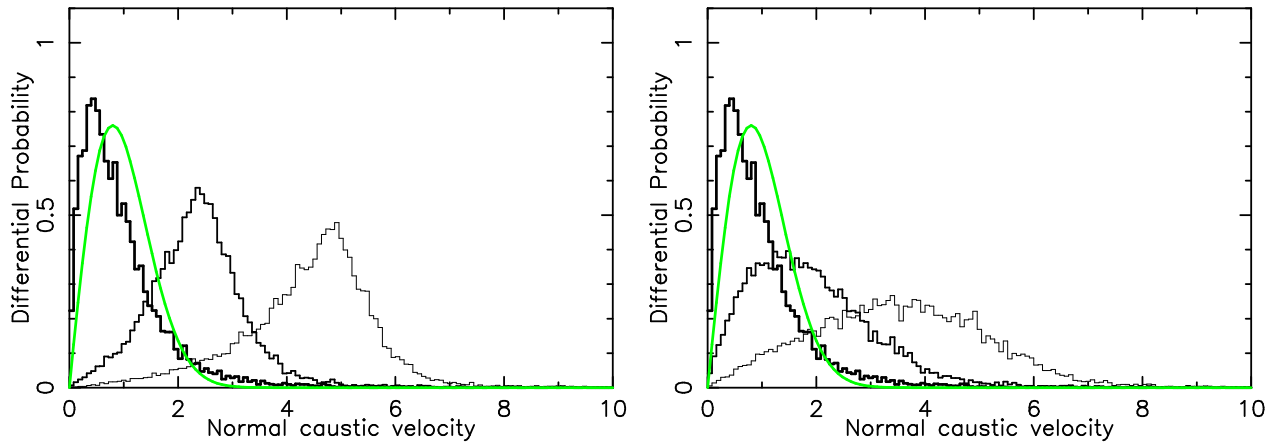


**Figure 2.** The probability distribution functions of normal caustic velocities. The thin, medium and thick lines correspond to transverse velocities of  $v_t = 0, 2.5$  and  $5 \times$  the average projected speed of the stellar velocity dispersion respectively. The thin light line shows the distribution of stellar speeds. Left: The applied shear is positive ( $\gamma > 0$ ). Right: The applied shear is negative ( $\gamma < 0$ ).

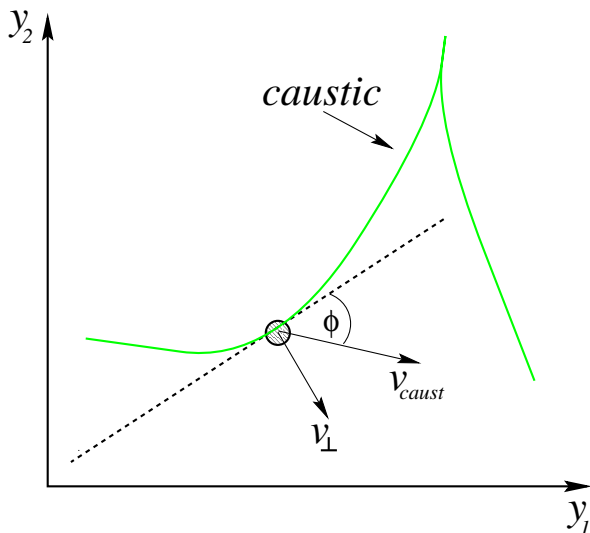


**Figure 1.** A schematic of the geometry of a caustic crossing a source.

for images C and D  $\sigma_{SE}=0.02$  mag. In the second case, a larger error was assumed (LE). For images A and B,  $\sigma_{LE}=0.02$  mag and for images C and D  $\sigma_{LE}=0.04$  mag. The observational error in Irwin et al. (1989) was 0.02 mag. The simulations employed in the determination of the effective transverse velocity assume a point source. For the current work 5000 sampled simulations were produced at each transverse velocity from the 100  $10\eta_o$  simulations for each model. The procedure for computing the cumulative probability ( $P_v(v_{tran} < V | \langle m \rangle)$ ) that the effective galactic transverse velocity is less than an assumed value (for a given microlens mass  $\langle m \rangle$ ) is described in Wyithe, Webster & Turner (1998c). The function  $P_v(v_{tran} < V | \langle m \rangle)$  was computed under two assumptions for the Bayesian prior and was found to be quantitatively consistent in those cases. These assumptions were of a flat ( $p_v(v_{tran}) \propto dv_{tran}$ ) and of a logarithmic ( $p_v(v_{tran}) \propto \frac{dv_{tran}}{v_{tran}}$ ) prior respectively.

The galactic transverse velocity is obtained from the effective transverse velocity by comparing the microlensing rates in terms of the histogram of light curve derivatives. The procedure is outlined in Wyithe, Webster & Turner (1999b).

There is a simple scaling that relates models of the same optical depth but consisting of model stars with a different mass. The dimensionless Einstein radius of a point mass is  $\sqrt{m}$ . If all masses in the model are reduced by a factor  $a$ , then all physical distances (in both the source and lens planes) between dimensionless coordinates are reduced by a factor  $\sqrt{a}$ . The gradient of the light-curve therefore scales as  $1/\sqrt{a}$ , and the measurement of effective transverse velocity that is made within the context of a given model through comparison with a data set is proportional to  $\sqrt{a}$ . However the distribution of caustic velocities that is produced from random proper motion is insensitive to the mean microlens mass. This scaling allows a microlensing model to be applicable to models with many different mean masses.

### 3 SOURCE SIZE

The HME in image A observed during late 1988 is described by 5 observations (Irwin et al. 1989; Corrigan et al. 1991) that constrain a peak in the light-curve. We assume that the length of the HME of is twice the estimated rise time of 26 days (Corrigan et al. 1991). To measure the size of the source continuum region we consider the observed event length of 52 days in light of the calculations of transverse velocity that we have made previously (Wyithe, Webster & Turner 1999b). We use these values of transverse velocity in combination with calculations of the normal caustic velocities that arise from the proper motion of stars, as well as the orientations of tangents to the caustic points.

The velocity of the caustic network resulting from the stream motion of a starfield was calculated by Schramm et al. (1993). This result was generalised by Kundic, Witt & Chang (1993) so that the velocity of individual caustic points due to the proper motion of stars could be determined. We use the expressions obtained to find the velocities of caus-

tic points in the  $y_1$  and  $y_2$  directions. The vector addition of these components is in general in a direction other than that which is normal to the caustic at that point. Therefore we also calculate the caustic gradient. The method of calculating both the caustic location and gradient are described below.

We implement the contouring algorithm as described by Lewis et al. (1993). The image curves are followed in discrete steps in one direction. During the contouring algorithm the occurrence of the image line crossing a critical curve results in the image magnification changing sign due to a parity flip between the critical images on either side of the critical curve. The location of the critical curve can then be found through a search for the image position that produces a lens mapping (Eqn 1) Jacobian determinant of zero. This value for the critical image position is used in the expressions for caustic velocity. The gradient of the caustic tangent is found by first computing the location of a point a short distance along the critical curve in both directions. The corresponding caustic points are then used to compute the gradient of the caustic tangent from a three-point derivative.

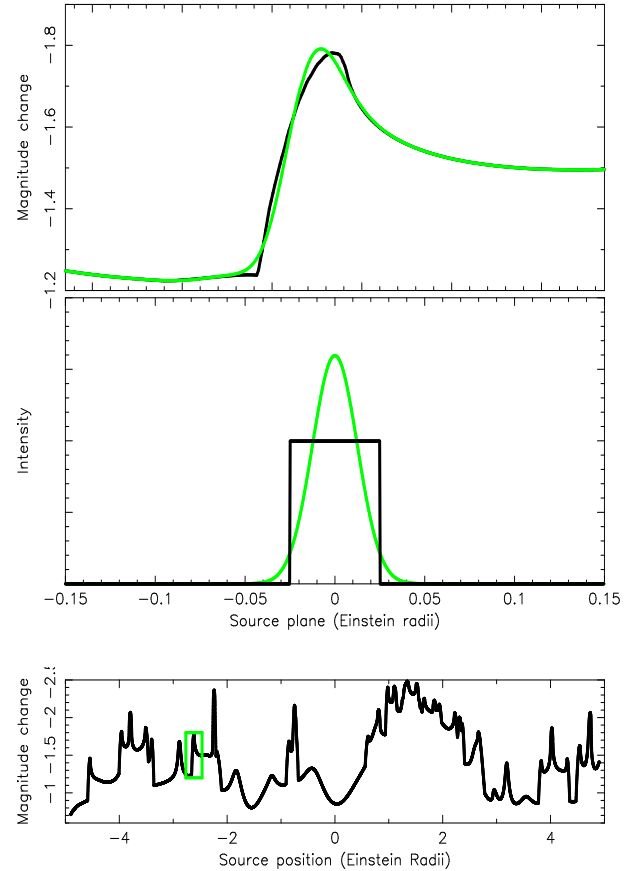
In each of the models considered we found the distribution of caustic velocities and gradients by searching for caustics along an equal length of source track in two orthogonal directions. The source tracks were each  $10\eta_o$  in length and were computed from a separate model starfield. We computed the properties of the caustics that intersect with 500 such source tracks in both the directions that are parallel ( $\gamma > 0$ ) and perpendicular ( $\gamma < 0$ ) to the shear. This is equivalent to finding the caustic locations on a  $500 \times 500$  line grid covering a  $10\eta_o \times 10\eta_o$  square of source plane, although the use of 1000 starfields makes the sample more statistically representative.

Figure 1 is a schematic representation of the determination of the normal caustic velocity from the caustic velocity and gradient. The caustic velocity is the vector addition of the transverse velocity ( $v_{tran1}, v_{tran2}$ ) and the contribution to caustic velocity that results from stellar proper motion ( $v_1, v_2$ ). The normal caustic velocity  $\vec{v}_\perp$  is computed from the components of the caustic velocity ( $\vec{v}_{caust} = (v_1 + v_{tran1}, v_2 + v_{tran2})$ ) in combination with the relative orientation between the tangent to the caustic and the caustic velocity vector. The magnitude of the normal caustic velocity is:

$$v_\perp = |\vec{v}_\perp| = |\vec{v}_{caust} \times \sin(\phi)|, \quad (2)$$

where  $\phi$  is the angle between the tangent to the caustic and the caustic velocity. A caustic that has a velocity which makes a small angle with the tangent to the caustic sweeps out a smaller area per unit length per unit velocity than one which has a velocity normal to its tangent. Therefore, to calculate the distribution of normal caustic velocities at a stationary source position, each value of  $v_\perp$  carries a weight of  $|\sin(\phi)|$ .

Figure 2 shows probability distributions of normal caustic velocities. All velocities on this plot are in units of the projected mean speed of the the stellar velocity dispersion. The left and right hand diagrams correspond to the cases of positive and negative galactic shear respectively. Distributions are shown in each case for the normal caustic velocities due to the stellar proper motions alone (thick line), and in combination with a transverse velocity in the  $y_1$  direc-



**Figure 3.** Bottom: A sample light-curve for image A ( $\gamma_A = +0.4$ ) of Q2237+0305. One half of a double peaked event is highlighted by a box and reproduced in the top panel. Centre: A top-hat intensity profile (dark line), and a Gaussian intensity profile (light line). Top: A plot of the the highlighted HME showing the details of the event shapes that result from the two source intensity profiles.

tion of 2.5 (medium line) and 5.0 (thin line). Also plotted in figure 2 is the distribution of stellar speeds (light line). These diagrams demonstrate the dependence of the mean normal caustic velocity on the direction of a transverse velocity. Note however that the result is independent of the sign of the shear in the case where there is no transverse velocity. When the transverse velocity is lined up with the direction of the caustic clustering ( $\gamma < 0$ ) the resulting normal caustic velocity is lower on average than when the transverse velocity is perpendicular to it ( $\gamma > 0$ ). This is because the tangent to the caustic is more likely to lie along the source trajectory.

For a small source ( $S_s \ll \eta_o$ ) the crossing time of the caustic is  $\Delta T = S_s/v_\perp$ , where  $S_s$  is the source diameter. Therefore, the dimension of the source in a direction normal to the caustic is

$$S_s = v_\perp \times \Delta T. \quad (3)$$

This expression demonstrates that there is a systematic uncertainty in our determination of source size that is proportional to the uncertainty in the estimate of the event length.

In this paper we assume that the projected source pro-

**Table 2.** Table showing the upper and lower 99%, 95%, and 90% limits as well as the mean of the distributions  $p_s(S_s | 0.1M_\odot)$  and  $p_s(S_s | 1.0M_\odot)$ . The values are given for the two directions assumed for the transverse velocity as well as for simulations that contain 0% and 50% smoothly distributed matter. The limits shown correspond to the cases where the error was  $\sigma_{SE} = 0.01$  mags in images A/B,  $\sigma_{SE} = 0.02$  mags in images C/D, and where the error was  $\sigma_{LE} = 0.02$  mags in images A/B,  $\sigma_{LE} = 0.04$  mags in images C/D (in parentheses).

0% Smooth Matter								
Mean Mass	Trajectory Direction	$S_{low}(99\%)$ ( $\times 10^{14} cm$ )	$S_{low}(95\%)$ ( $\times 10^{14} cm$ )	$S_{low}(90\%)$ ( $\times 10^{14} cm$ )	Mean ( $\times 10^{14} cm$ )	$S_{up}(90\%)$ ( $\times 10^{14} cm$ )	$S_{up}(95\%)$ ( $\times 10^{14} cm$ )	$S_{up}(99\%)$ ( $\times 10^{14} cm$ )
$0.1M_\odot$	$\gamma_A, \gamma_B > 0$	0.244 (0.238)	0.637 (0.617)	1.01 (0.972)	6.70 (6.52)	12.1 (11.9)	16.6 (16.2)	29.2 (29.0)
$1.0M_\odot$	$\gamma_A, \gamma_B > 0$	0.394 (0.280)	1.10 (0.746)	1.80 (1.19)	12.7 (8.48)	24.1 (16.0)	31.3 (21.7)	49.2 (36.6)
$0.1M_\odot$	$\gamma_C, \gamma_D > 0$	0.240 (0.237)	0.622 (0.614)	0.982 (0.968)	6.56 (6.50)	11.9 (11.9)	16.3 (16.2)	29.1 (29.0)
$1.0M_\odot$	$\gamma_C, \gamma_D > 0$	0.370 (0.272)	1.03 (0.723)	1.67 (1.16)	11.9 (8.11)	22.6 (15.2)	29.2 (20.5)	46.0 (35.1)

50% Smooth Matter								
Mean Mass	Trajectory Direction	$S_{low}(99\%)$ ( $\times 10^{14} cm$ )	$S_{low}(95\%)$ ( $\times 10^{14} cm$ )	$S_{low}(90\%)$ ( $\times 10^{14} cm$ )	Mean ( $\times 10^{14} cm$ )	$S_{up}(90\%)$ ( $\times 10^{14} cm$ )	$S_{up}(95\%)$ ( $\times 10^{14} cm$ )	$S_{up}(99\%)$ ( $\times 10^{14} cm$ )
$0.1M_\odot$	$\gamma_A, \gamma_B > 0$	0.207 (0.187)	0.556 (0.493)	0.895 (0.795)	5.95 (5.31)	11.1 (9.75)	14.6 (13.3)	24.0 (23.2)
$1.0M_\odot$	$\gamma_A, \gamma_B > 0$	0.487 (0.274)	1.45 (0.772)	2.48 (1.26)	16.4 (10.1)	30.1 (19.4)	38.1 (25.7)	58.4 (40.4)
$0.1M_\odot$	$\gamma_C, \gamma_D > 0$	0.206 (0.188)	0.553 (0.495)	0.888 (0.796)	5.73 (5.27)	10.5 (9.57)	13.1 (13.2)	23.3 (23.0)
$1.0M_\odot$	$\gamma_C, \gamma_D > 0$	0.468 (0.272)	1.36 (0.760)	2.26 (1.23)	14.5 (9.25)	26.8 (17.7)	33.7 (23.2)	49.3 (36.7)

file is circular so that the event time is not dependent on the source orientation. Eqn 3 defines our measure of source size. The interpretation of this size however is dependent on the profile of the source. The lower panel in figure 3 shows an example of an extended source light-curve for image A ( $\gamma_A = +0.4$ ) computed using the method described in Wyithe & Webster (1999). One half of a double peaked event in this light-curve is highlighted by a box. This event is reproduced in the top panel of figure 3 for two source intensity profiles, a Gaussian profile (light line) and a top-hat profile (dark line). Cross-sections of these intensity profiles are shown in the central panel of figure 3 with a scale equal to that which produced the HME. This figure demonstrates that if the source profile was described by a top-hat function then  $S_s$  is approximately the source diameter. However, if the profile is Gaussian then the measured radius will be approximately twice its half width.

Limits on the source size are obtained from Eqn 3 by considering the distribution of the normal caustic velocity in combination with the observed event length. To obtain the distribution of source size,  $p_s(S_s | \langle m \rangle)$  we integrate the probability distributions for caustic velocity at a given transverse velocity,  $p_c(v_\perp | \langle m \rangle, v_{tran})$  over the probability distribution of transverse velocity,  $p_v(v_{tran} | \langle m \rangle)$ .  $p_v(v_{tran} | \langle m \rangle)$  is obtained from the derivative of the cumulative distribution,  $P_v(v_{tran} < V | \langle m \rangle)$  following the correction for the contribution of stellar proper motion to the value of effective transverse velocity (Wyithe, Webster & Turner 1999b). The expression for  $p_s(S_s | \langle m \rangle)$  is

$$p_s(S_s | \langle m \rangle) = \frac{1}{\Delta t} \int p_c(v_\perp | \langle m \rangle, v_{tran}) p_v(v_{tran} | \langle m \rangle) dv_{tran}. \quad (4)$$

### 3.1 Determination of source size

The results of our source size estimates are presented in Figures 4 and 5, and Table 2. Values are given that correspond to assumed mean microlens masses of  $0.1M_\odot$  and  $1.0M_\odot$ . Figures 4 and 5 show cumulative and differential distributions of source size  $P_s(S_s < R | 0.1M_\odot)$  (thin lines),  $P_s(S_s < R | 1.0M_\odot)$  (thick lines), and  $p_s(S_s | 0.1M_\odot)$  (thin lines),  $p_s(S_s | 1.0M_\odot)$  (thick lines). The solid and dotted lines correspond to the cases where the photometric error was assumed to be  $\sigma_{SE}=0.01$  mag in images A/B and  $\sigma_{SE}=0.02$  in images C/D, and  $\sigma_{LE}=0.02$  mag in images A/B and  $\sigma_{LE}=0.04$  in images C/D respectively. Table 2 shows the upper and lower 99%, 95%, and 90% limits as well as the mean of the distributions  $p_s(S_s | 0.1M_\odot)$  and  $p_s(S_s | 1.0M_\odot)$ . The values are given for the two directions assumed for the transverse velocity as well as for simulations that contain 0% and 50% smoothly distributed matter. The limits are shown corresponding to the cases where the error was  $\sigma_{SE} = 0.01$  mags in images A/B,  $\sigma_{SE} = 0.02$  mags in images C/D, and where the error was  $\sigma_{LE} = 0.02$  mags in images A/B,  $\sigma_{LE} = 0.04$  mags in images C/D (in parentheses). We find that the source size lies between the values of  $2 \times 10^{13} cm$  and  $6 \times 10^{15} cm$  (98% level).

The values obtained demonstrate that while the measured lower limit of source size is not very sensitive to the mass assumed for the model, the upper limit is larger when a higher mean microlens mass is assumed. This trend is demonstrated in figures 4 and 5, and can be understood as follows. The limit of effective transverse velocity measured is proportional to  $\sqrt{\langle m \rangle}$  and therefore has a value that is more likely to be low or zero for lower assumed values of mean microlens mass. The lower limits of source size come from the lowest velocity caustics, and these are produced by the stellar proper motions alone, hence the insensitivity to the microlens mass. However the upper limits are produced from the fastest moving caustics. These are a result of the com-

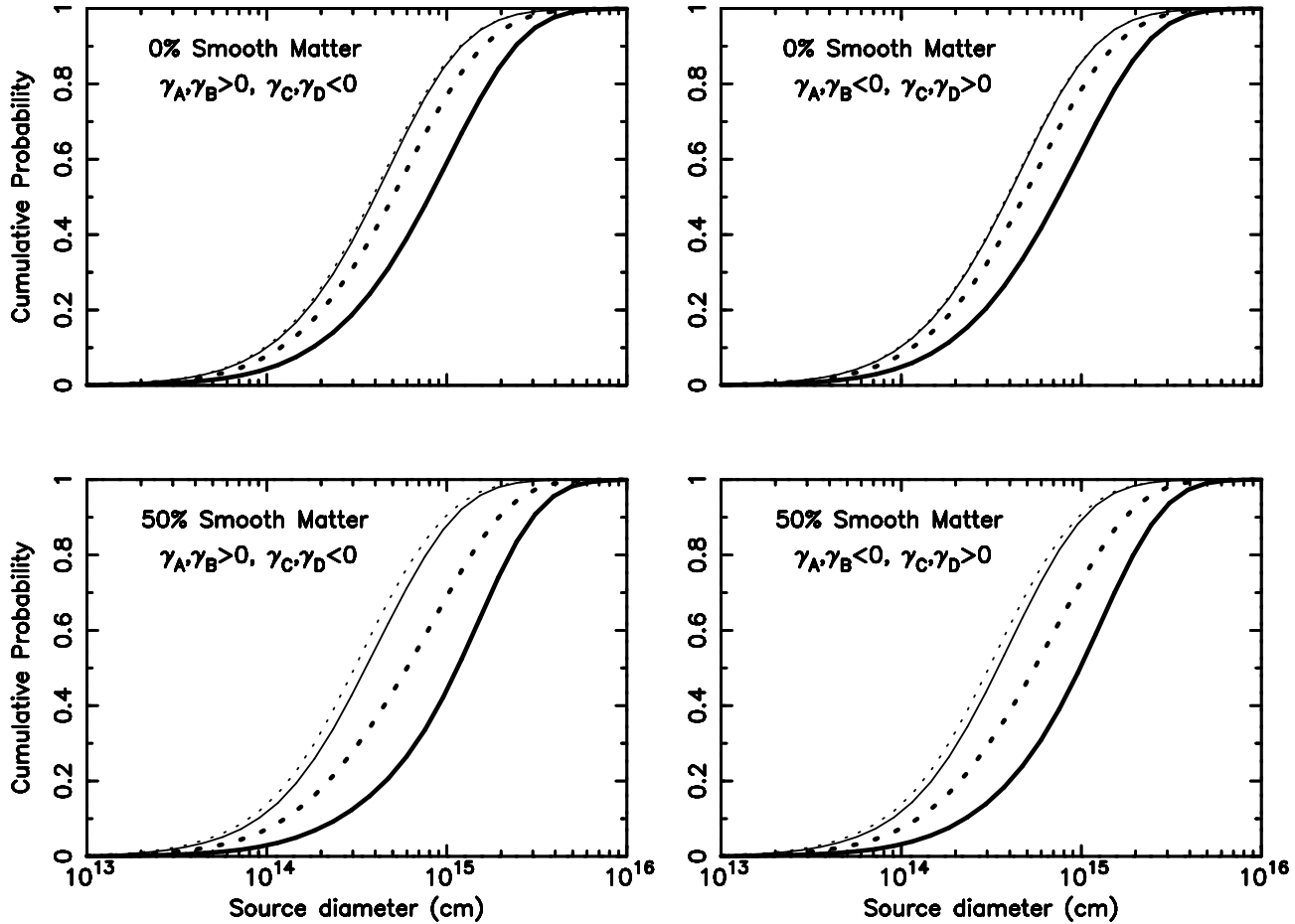


**Figure 4.** The cumulative distributions of source size  $P_s(S_s < R | 0.1M_\odot)$  (thin lines) and  $P_s(S_s < R | 1.0M_\odot)$  (thick lines). The solid and dotted curves represent the resulting functions when the photometric error was assumed to be  $\sigma_{SE}=0.01$  mag in images A/B and  $\sigma_{SE}=0.02$  in images C/D, and  $\sigma_{LE}=0.02$  mag in images A/B and  $\sigma_{LE}=0.04$  in images C/D.

bination of the stellar proper motions with the upper limits to transverse velocity. The upper limits are mass dependent and hence so to are the upper limits to source size. This effect is magnified in the smooth matter case. The transverse velocity that is measured by a model that contains smoothly distributed matter is larger than that measured by one containing only point masses. This is due to the more sparsely distributed caustic network and the more linear nature of the fold caustics (Wyithe, Webster & Turner 1999c). The upper limit of source size that is measured is therefore more dependent on the mass assumed if the model smooth matter content is higher.

As mentioned, there is an increased probability for high velocity caustics in the case where the assumed mass is higher. The mean of the source size distribution therefore increases with mass. However because the most likely transverse velocity is low, the lower end of the distribution is independent of the mass assumed. The resulting source size distribution is therefore highly asymmetric. In addition the mode is between  $\sim 1 \times 10^{14}$  cm and  $4 \times 10^{14}$  cm for all models considered.

It is apparent from figures 4 and 5 that the size of the photometric error assumed is an important factor in the de-

termination of the limits on source size. The effect of the size of the error is however more significant where the assumed mean mass is higher. This is because the error effects the measurement of transverse velocity, a factor that contributes to the high velocity caustics and hence to the large source size measurements. Once again the resulting variation in transverse velocity measurement does not significantly effect the determination of the lower limits as these are produced by caustic velocities that result from stellar proper motion. The effect is more significant upon the introduction of smooth matter into the models since there is then a larger discrepancy between the measured effective transverse velocity and the equivalent transverse velocity.

Both the lower and upper limits of source size are insensitive to the direction assumed for the transverse velocity when the assumed microlens mass is  $0.1M_\odot$ . This is because the most likely transverse velocity is zero so that the caustic velocities are produced by stellar proper motions. However if the mass is assumed to be  $1.0M_\odot$  then while the lower limit remains insensitive, the upper limits vary due to the variation in the measurement of transverse velocity.

The co-dependence of mean microlens mass and source size is now treated more rigorously.

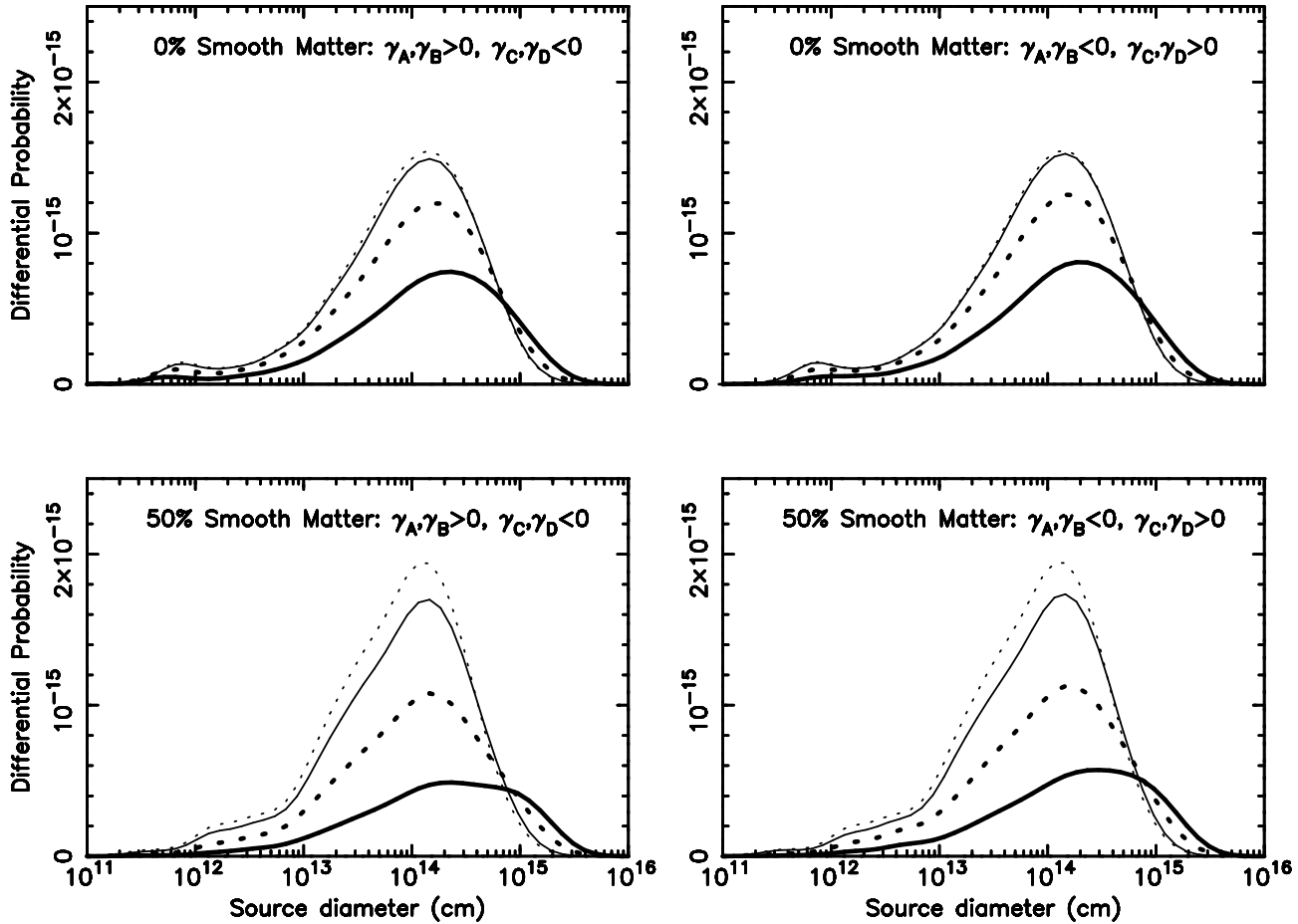


Figure 5. The differential distributions of source size  $p_s(S_s | 0.1M_\odot)$  (thin lines) and  $p_s(S_s | 1.0M_\odot)$  (thick lines). The solid and dotted curves represent the resulting functions when the photometric error was assumed to be  $\sigma_{SE}=0.01$  mag in images A/B and  $\sigma_{SE}=0.02$  in images C/D, and  $\sigma_{LE}=0.02$  mag in images A/B and  $\sigma_{LE}=0.04$  in images C/D.

### 3.2 Simultaneous limits of mean microlens mass and source size

In Sec. 3.1 the normalised probability distributions,  $p_s(S_s | \langle m \rangle)$ , that the continuum source size is between  $S_s$  and  $S_s + dS_s$  given that the mean microlens mass is  $\langle m \rangle$ , were obtained. The probability that the source size lies in the above range and the mean microlens mass is between  $\langle m \rangle$  and  $\langle m \rangle + d\langle m \rangle$  is then given by

$$p_{m,s}(S_s, \langle m \rangle) = p_s(S_s | \langle m \rangle) p_m(\langle m \rangle), \quad (5)$$

where  $p_m(\langle m \rangle)$  is the probability that the mean microlens mass is between  $\langle m \rangle$  and  $\langle m \rangle + d\langle m \rangle$ .  $p_m$  is a known function, given in Wyithe, Webster & Turner (1999c), that is approximately independent of the source size.  $p_m(\langle m \rangle)$  was determined under the same assumptions of the Bayesian prior for the galactic transverse velocity as the function  $p_v(v_{tran})$ , however unlike  $p_v(v_{tran})$ ,  $p_m(\langle m \rangle)$  is dependent on the prior assumed.

Figure 6 shows contour plots of the two-dimensional distribution  $p_{m,s}$  for the assumed source orientations, smooth matter fraction and photometric errors. All possible combinations of the two values of each parameter are included, so that eight models are shown. The contours are at 3.6, 14,

26, 61 per cent of the peak height, and so the extrema of the relevant contours represent  $4\sigma$ ,  $3\sigma$ ,  $2\sigma$ , and  $1\sigma$  limits on the single variables. The light and dark lines correspond to the assumptions of logarithmic and flat priors for transverse velocity. The most likely model is that  $\langle m \rangle \simeq 0.05 - 0.2M_\odot$  (dependent on the content of smooth matter assumed) and  $S_s \simeq 2 \times 10^{14}$  cm (independent of model).

The most important benefit of combining the distributions of  $S_s$  and  $\langle m \rangle$  is that an upper limit can be placed on the mean microlens mass. The limits on  $\langle m \rangle$  are subject to both random and systematic uncertainties, with the measured mass increasing with photometric errors and decreasing with the fraction of smooth matter. Assuming that the chosen values for these parameters bracket the likely models, upper and lower limits for  $\langle m \rangle$  can be found by using the most extreme values of the contour limits. This yields the 95 per cent result that  $0.01M_\odot \lesssim \langle m \rangle \lesssim 1M_\odot$ . The upper limit is lower than that obtained by Lewis & Irwin (1996), although sufficiently high that it does not conflict with any popular models of galactic halos or bulges. Similarly, the contour maxima yield the result that there is a 95 per cent chance that  $5 \times 10^{12}$  cm  $\lesssim S_s \lesssim 10^{15}$  cm. At a given confidence level, both the upper and lower limits of

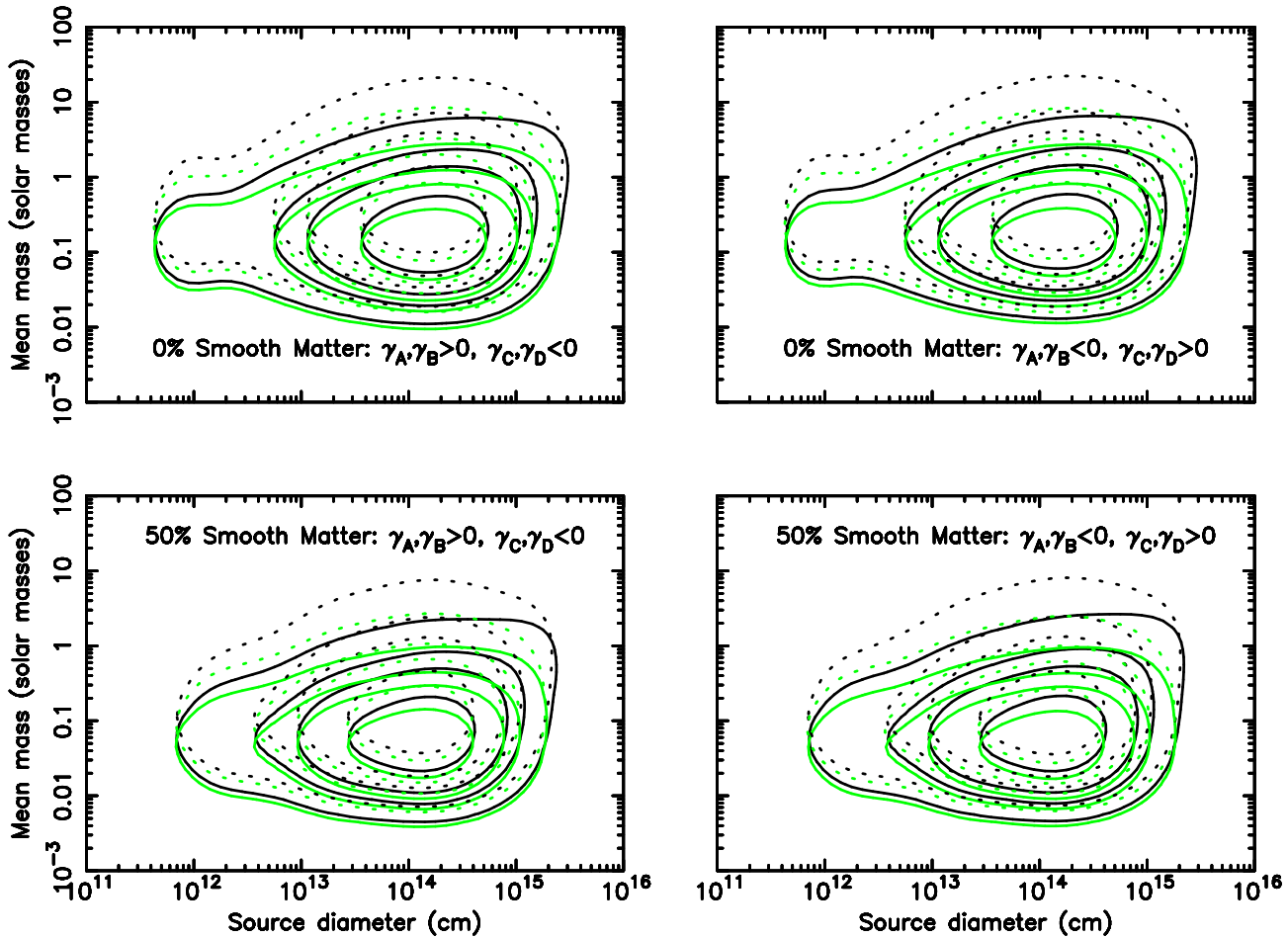


**Figure 6.** Contours of percentage peak height of the function  $p(S_s, \langle m \rangle)$ . The contours shown are the 3.6%, 14%, 26% and 61% levels. The solid and dotted curves represent the resulting functions when the photometric error was assumed to be  $\sigma_{SE}=0.01$  mag in images A/B and  $\sigma_{SE}=0.02$  in images C/D, and  $\sigma_{LE}=0.02$  mag in images A/B and  $\sigma_{LE}=0.04$  in images C/D. The light and dark lines correspond to the assumptions of logarithmic and flat priors for transverse velocity referred to in the text.

source size, and the lower limit of mean microlens mass have smaller values in Figure 6 than those obtained in previous sections and Wyithe, Webster & Turner (1999c). This can be attributed to the asymmetric nature of the distribution in both dimensions.

#### 4 CONCLUSION

The observed peak in the light-curve of image A of Q2237+0305 in 1988 appears to be one half of a double peaked event that is characteristic of a source having passed inside of a cusp. If this interpretation is correct then the observed peak is the result of the source having been crossed by a single caustic. The observations therefore provide a good record of the caustic crossing time. The source size is the product of the event length and the normal velocity of the caustic involved. We have placed limits on normal caustic velocities by combining measurements of the galactic transverse velocity based on the entire set of published monitoring data with calculations of the distributions of caustic gradients as well as the component of the caustic velocities that result from stellar proper motions. We find

that the most likely size of the magnified continuum region is  $S_s \sim 2 \times 10^{14}$  cm, and that the upper and lower limits are  $S_s \sim 6 \times 10^{15}$  cm and  $S_s \sim 2 \times 10^{13}$  cm (99% level) respectively. Simultaneous consideration of microlens mass and source size has provided an upper limit to the mean microlens mass of  $1M_\odot$  that was unavailable from consideration of the microlensing rate alone.

It was noted in Wyithe, Webster & Turner (1999b) that the statistical determination of the effective transverse velocity will be aided when monitoring data from a longer period becomes available. The narrowing of the likelihood for the effective transverse velocity will in turn provide tighter limits on the mean microlens mass and source size. At a known transverse velocity, the component of uncertainty due to the range of event lengths that can be produced by a source will be reduced upon the observation of more HME durations. Thus the extent of the contours in figure 6 will be reduced as more monitoring data becomes available.

#### REFERENCES

Chang, K., Refsdal, S., 1979, *Nature*, 282, 561

- Corrigan et.al, 1991, *Astron. J.*, 102, 34
- Foltz, C. B., Hewitt, P. C., Webster, R. L., Lewis, G. F., 1992, *Ap. J.*, 386, L4 3
- Irwin, M. J., Webster, R. L., Hewitt, P. C., Corrigan, R. T., Jędrzejewski, R. I., 1989, *Astron. J.*, 98, 1989
- Jaroszynski, M., Wambsganss, J., Paczynski, B., 1992, *Ap. J.*, 396, L65
- Kent, S. M., Falco, E. E., 1988, *Astron. J.*, 96, 1570
- Kundic, T., Witt, H. J., Chang, K., 1993, *Ap. J.*, 409, 537
- Lewis, G. F., Irwin, M. J., 1996, *MNRAS* 283, 225
- Lewis, G. F., Irwin, M. J., Hewitt, P. C., Foltz, C. B., 1998, *MNRAS*, accepted
- Lewis, G. F., Miralda-Escude, J., Richardson, D. C., Wambsganss, J., 1993, *MNRAS*, 261, 647
- Østensen, R. et al. 1996, *Astron. Astrophys.*, 309, 59
- Rauch, K. P., Blandford, R. D., 1991, *Ap. J.* 1991, 381, L39
- Schmidt, R. W., Webster, R. L., Lewis, G. F. 1998, *MNRAS*, 295, 488
- Schneider, D. P., Turner, E. L., Gunn, J. E., Hewitt, J. N., Schmidt, M., Lawrence, C. R., 1988, *Astron. J.*, 95, 1619
- Schramm, T., Kayser, R., Chang, K., Nieser, L., Refsdal, S., 1993, *Astron. Astrophys.*, 268, 350
- Wambsganss, J., Paczynski, B., Schneider, P., 1990, *Ap. J.*, 358, L33
- Webster, R. L., Ferguson, A. M. N., Corrigan, R. T., Irwin, M. J., 1991, *Astron. J.*, 102, 1939
- Witt, H. J., 1990, *Astron. Astrophys.*, 236, 311
- Witt, H. J., 1993, *Ap. J.*, 403, 530
- Witt, H. J., Kayser, R., & Refsdal, S. 1993, *Astron. Astrophys.*, 268, 501
- Witt, H. J., Mao, S., 1994, *Ap. J.*, 429, 66
- Wyithe, J. S. B, Webster, R. L., 1999, *MNRAS* accepted
- Wyithe, J. S. B, Webster, R. L., Turner, E. L., 1999a, *MNRAS* submitted
- Wyithe, J. S. B, Webster, R. L., Turner, E. L., 1999b, *MNRAS* accepted
- Wyithe, J. S. B, Webster, R. L., Turner, E. L., 1999c, *MNRAS* submitted